Neuroscience 214 (2012) 1–13

STRENGTH–DURATION RELATIONSHIP FOR INTRA- VERSUS EXTRACELLULAR STIMULATION WITH MICROELECTRODES

F. RATTAY, [a]* **L. P. PAREDES** [a] **AND R. N. LEAO** [b,c]

[a] *Institute for Analysis and Scientific Computing, Vienna University of Technology, A-1040 Vienna, Austria*

[b] *Neurodynamics Laboratory, Department of Neuroscience, Uppsala University, Uppsala, Sweden*

[c] *Brain Institute, Federal University of Rio Grande do Norte, Natal-RN, Brazil*

Abstract—Chronaxie, a historically introduced excitability time parameter for electrical stimulation, has been assumed to be closely related to the time constant of the cell membrane. Therefore, it is perplexing that significantly larger chronaxies have been found for intracellular than for extracellular stimulation. Using compartmental model analysis, this controversy is explained on the basis that extracellular stimulation also generates hyperpolarized regions of the cell membrane hindering a steady excitation as seen in the intracellular case. The largest inside/outside chronaxie ratio for microelectrode stimulation is found in close vicinity of the cell. In the case of monophasic cathodic stimulation, the length of the primarily excited zone which is situated between the hyperpolarized regions increases with electrode–cell distance. For distant electrodes this results in an excitation process comparable to the temporal behavior of intracellular stimulation. Chronaxie also varies along the neural axis, being small for electrode positions at the nodes of Ranvier and axon initial segment and larger at the soma and dendrites. As spike initiation site can change for short and long pulses, in some cases strength–duration curves have a bimodal shape, and thus, they deviate from a classical monotonic curve as described by the formulas of Lapicque or Weiss. **© 2012 IBRO. Published by Elsevier Ltd. All rights reserved.**

Key words: chronaxie, strength–duration curve, electrical stimulation, microelectrode, activating function.

INTRODUCTION

Selective neural stimulation is a great challenge in the development of neural prostheses. As an example, active contacts of an electrode array implanted at the retina or other structures along the visual pathway should stimulate elements that elicit visual sensations corresponding to the place in the array (Brindley, 1955; Zrenner, 2002; Dowling, 2005; Fernández et al., 2005; Fried et al., 2006; Cohen, 2007; Sekirnjak et al., 2008; Horsager et al., 2009; Pezaris and Reid, 2009; Tehovnik et al., 2009) while avoiding side effects like co-stimulation of bypassing axons arising from distant locations (Greenberg et al., 1999; Rattay and Resatz, 2004). Considering the fact that neural substructures have different strength–duration characteristics may give an opportunity for more selective stimulation. For example, in the treatment of chronic pain during spinal cord stimulation smaller dorsal column fibers can only be activated when pulse width is sufficiently large (Holsheimer et al., 2011).

Recently, the strength–duration relationship for extracellular neural stimulation was analyzed under the assumption of a constant electrical field in flat, spherical and cylindrical cells (Boinagrov et al., 2010). These investigations provided a biophysical basis for the stimulation with large electrodes and also explained effects of stimulation with ultrashort pulses (<5 μs). In accordance with retinal ganglion cell experiments (Jensen et al., 2005), for pulse durations <2 ms, it was found that a 500 μm diameter electrode placed above the soma caused excitation with significantly lower thresholds compared to a position above the axon. This result is unexpected given the assumption that the axon is the most excitable part of a neuron externally stimulated (Nowak and Bullier, 1998; Rattay, 1999). Differences in experimental setups are the reason for the controversy about such observations. Stimulation of the retina with large electrodes generates a rather constant field and consequently transverse currents depolarize the cell membrane at one side and hyperpolarize the cell at the opposite side. On the other hand, external excitation with small electrodes is mainly based on stimulating effects resulting from extracellular potential variations along the neural structure (Rushton, 1927; Ranck, 1975; Rattay, 1986, 1987, 1999). These facts vary the expected excitation paradigm and should be carried in mind.

Voltage sensitive ion channel types and densities are other important elements for neuron excitability. In relation to retinal implant, electrode positions applied at a dense two-dimensional grid around the soma region of rabbit ganglion cells showed the lowest thresholds along a small section of the axon, about 40 μm from the soma. At this axonal section, immunochemical staining revealed a dense band of voltage-gated sodium channels (Fried et al., 2009). Similarly, high sodium channel densities at the axon initial segments (AIS) of cortical cells define sites for action potential initiation under natural conditions (Stuart et al., 1997; Yu et al., 2008; Hu et al., 2009) as well as spike initiation candidates for external stimulation with microelectrodes (Rattay and Wenger, 2010).

*Corresponding author. Tel: +43-1-58801-10114.
E-mail address: frank. rattay@tuwien. ac. at (F. Rattay).
Abbreviations: AIS, axon initial segments; VSD, voltage sensitive dye.

0306-4522/12 $36.00 © 2012 IBRO. Published by Elsevier Ltd. All rights reserved.
http://dx.doi.org/10.1016/j.neuroscience.2012.04.004

A strength–duration curve describes electrode threshold current as function of stimulus pulse duration. Chronaxie is defined as the time on such a strength–duration curve for twice the minimum (rheobase) current needed for very long pulses. Established by experimental findings, this excitability parameter was assumed to be rather independent from the distance between the current source and the excited cell (Weiss, 1901; Lapicque, 1907, 1929; Blair, 1932).

As different neural structures have different chronaxies, stimulus pulse duration is an important element for selective stimulation as well as for electrophysiological classification. For example, the shorter chronaxie of myelinated motorneurons compared to that of unmyelinated fibers of the myocardium allows safe stimulation with short pulses during artificial respiration. Motoneurons then become activated with little disturbance of the myocardial function (Voorhees et al., 1992). In electrophysiological studies, extracellular gray matter stimulation shows larger chronaxies for somas than for axons, supporting the idea that spike initiation occurs in the axon (Nowak and Bullier, 1998). Additionally, in cochlear implants, significantly shorter chronaxies have been described in long-term (compared to acute) deafened cochleae, indicating the loss of peripheral processes in many spiral ganglion cells (Shepherd et al., 2001).

Based on theoretical considerations, chronaxie has been suggested to be about 0.7 times the time constant of the cell membrane (Blair, 1932; Ranck, 1975; Reilly, 1992). Therefore, some authors assume chronaxie as independent of in- or outside stimulation of the cell (Nowak and Bullier, 1998). This hypothesis contrasts with reports of considerably larger chronaxies for intracellular than for extracellular stimulation (Ranck, 1975).

Discrepancy among different works prompts speculations that experimental differences could be caused by artifacts like sampling errors or neuronal damage during recordings (Ranck, 1975). To address this controversy, we systematically reproduced experimental findings using computer simulations of a pyramidal cell and its simplified rectified version for electrode positions at the dendrite, the soma, the lateral ending of the AIS and the myelinated axon (Fig. 1). In all cases shown in Fig. 1B, the intracellular/extracellular chronaxie ratio is two or higher. It is

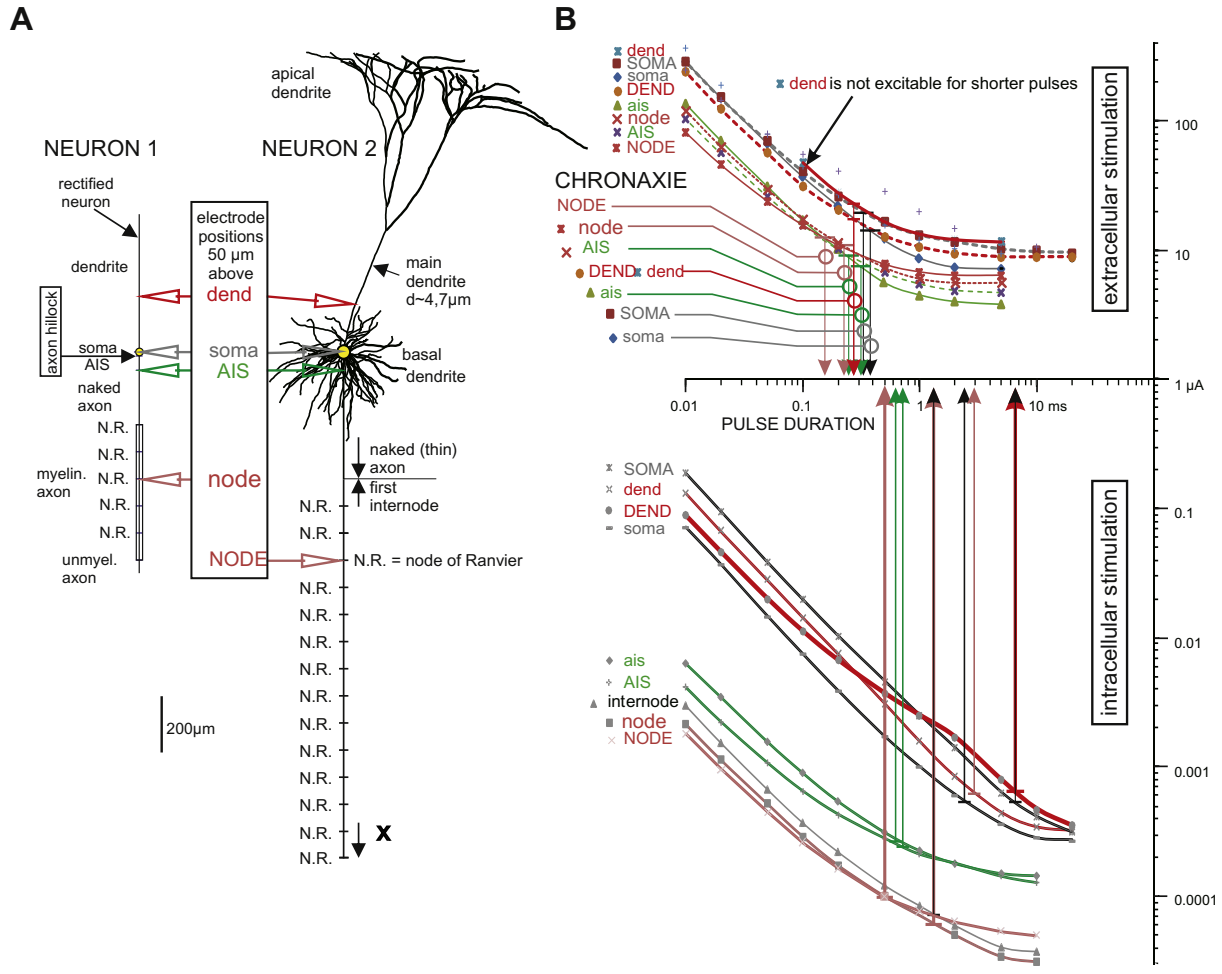

Fig. 1. Strength–duration curves of the investigated pyramidal cell. (A) Neuron 1 (left) and Neuron 2 (right) with selected electrode positions. (B) Strength–duration curves with chronaxie values for electrode positions as marked in A. Lower and upper case letters are used for electrode positions for Neuron 1 and Neuron 2, respectively. Color coding of lines in B corresponds to electrode positions in A. For better discrimination some extracellular strength–duration curves are shown as broken lines. Colors of break point markers are without meaning. Anodic and cathodic square pulses for intra- and extracellular stimulation, respectively.

important to note that these ratios depend on cell properties as well as on the distance and type of electrodes. Such variants could be the reason for the diversity in chronaxie data.

Here, we demonstrate that (i) hyperpolarized regions are responsible for the shorter extracellular chronaxies, (ii) for short electrode distances, excitability and chronaxie differ essentially along a selected neuron and consequently (iii) strength duration curves are expected to deviate from the classical form when short and long pulses cause action potential initiation at sites with different electrical membrane properties.

EXPERIMENTAL PROCEDURES

An analysis of two model neurons is presented. In both models excitation is based on recently measured densities of high threshold sodium channels Nav1.2 in dendrites and the soma and low threshold sodium channels Nav1.6 in the axon (Hu et al., 2009). The phenomenon of short chronaxies for extracellular stimulation was also tested in simulations with other neural structures (not shown) and did not depend on the specific examples.

Model Neuron 1 (Fig. 1A left, Rattay and Wenger, 2010), a simplification of Neuron 2 concerning geometry and ion channel types, is straightforward to analyze and with less computational cost. It has a straight axis and consists of a single non-branching dendrite (500 μm, d = 5 μm), spherical soma (d = 20 μm), axon hillock (10 μm, d = 3.1 μm), AIS (50 μm, d = 1.22 μm), naked axon (unmyelinated, 200 μm, d = 1 μm), myelinated axon (500 μm, d = 1 μm) and unmyelinated terminal (50 μm, d = 1 μm). Assumptions for ion channel distribution and ion current computations are quite similar as in Hu et al. (2009): the same constant Nav1.2 channel density for the dendrite and soma (gna = 8 mS/cm^2), but 40 times higher sodium channel density in hillock and AIS with a change to the low threshold type Nav1.6 in the axon. Intracellular resistivity is 150 Ω cm, membrane capacity c = 1 μF/cm^2. Using ACSL (Advanced Continuous Simulation Language) software, Neuron 1 is simulated by evaluating the compartment model equations (1)–(3) as described below.

Model Neuron 2 (Fig. 1A right) is based on geometrical parameters of a traced cortical layer 5 pyramidal cell with ion channel assumptions as available in the NEURON (Carnevale and Hines, 2006) Model DB (Hines et al., 2004; Hu et al., 2009). In contrast to Neuron 1, soma diameter is increased to 30 μm, naked axon diameter is reduced to 0.4 μm and the capacity of the cell membrane of all compartments with exception of the soma and internodes is reduced to 0.5 μF/cm^2. Moreover, Neuron 2 incorporates branching dendrites, tapering diameters, uneven ion channel distribution within compartments of a single type and a membrane capacity of 0.02 μF/cm^2 in the axonal internodes. High threshold sodium Nav1.2, low threshold Nav1.6 and fast voltage-gated K^+ of Neuron 1 are complemented by slow non-inactivating potassium current, high-voltage activated Ca^{2+} and calcium dependent K^+ in dendritic and somatic compartments. All parameters are used as in Hu et al. (2009). However, in order to demonstrate current–distance relations in a clear way, the axial 3d structure of the cell was compressed into the x–y plane. Neuron 2 is simulated with NEURON.

In more detail, Neuron 1 soma and dendrite were implemented with the same constant maximum conductances (in mS/cm^2) $g_{Nav1.2}$ = 8, $g_{Nav1.6}$ = 0 and g_{Kv} = 10, the axon hillock with $g_{Nav1.2}$ = 320, $g_{Nav1.6}$ = 0, g_{Kv} = = 100, the AIS with $g_{Nav1.2}$ = 100, $g_{Nav1.6}$ = 320, g_{Kv} = 100, the unmyelinated axon with $g_{Nav1.2}$ = 0, $g_{Nav1.6}$ = 300, g_{Kv} = 150 and the nodes of Ranvier with $g_{Nav1.2}$ = 0, $g_{Nav1.6}$ = 160, g_{Kv} = 20. Sodium current kinetics are calculated by $I_{Nav1.j} = g_{Nav1.j} m^3 h (V - E_{Na})$ with j equals to either 2 or 6 and E_{Na} = 60 mV. Details on the differential equations of the different variables are shown in Mainen et al. (1995). The values for the half (in)activation voltages $V_{1/2}$, the slopes k and the coefficients A were obtained from a previously published model in the NEURON Model DB (Hu et al., 2009) after subtracting the corresponding value for the shift of voltage dependence of the kinetics. Consequently, the currents $I_{Nav1.j}$ have the same values for A, i.e., $A(\alpha_m)$ = 0.182, $A(\beta_m)$ = 0.124, $A(\alpha_h)$ = 0.024, $A(\beta_h)$ = 0.0091, and the slope of inactivation, i.e., $k(\tau_h)$ = 5 and $k(h_\infty)$ = 6.2, in contrast to altered slope of activation, i.e., $k(\tau_m) = k(m_\infty)$ = 7 for Na_v1.2 but $k(\tau_m) = k(m_\infty)$ = 6 for Na_v1.6. To account for the reduced threshold of Na_v1.6 channels $V_{1/2}(m)$ is decreased to −41 mV compared to the calculated value of −28 mV for activation of Na_v1.2 channels. The corresponding values in mV for the inactivation of Na_v1.2/Na_v1.6 channels are $V_{1/2}(\alpha_h)$ = −35/−41, $V_{1/2}(\beta_h)$ = −60/−73, $V_{1/2}(h_\infty)$ = −57/−70. The potassium currents are determined by $I_K = g_K n (V - E_K)$ with E_K = −90 mV. To be consistent the corresponding values of $A(\alpha)$ = 0.02, $A(\beta)$ = 0.002, $V_{1/2}(\alpha) = V_{1/2}(\beta)$ = 25 mV and $k(\alpha) = k(\beta)$ = 9 were also obtained from the NEURON Model DB (Hu et al., 2009). Internodes are simulated with 17 sheets of membrane with a conductance of 1 mS/cm^2 and C = 1 μF/cm^2 per sheet (Rattay, 1999). The presented results are simulated for 37 °C.

In the first modeling step, the extracellular potential V_e generated by an electrode tip is approximated considering a monopolar spherical electrode in an infinite homogeneous extracellular medium with resistivity ρ_e = 300 Ω cm. This is equivalent to a point source stimulation resulting in spherical isopotentials with $V_e = \rho_e I_{el}/4\pi r$ when a current pulse with amplitude I_{el} is applied; r is the distance from a point of interest to the point source.

In the second step, the response of a neuron is simulated by a compartment model. That is a network of resistances and capacitances, where the current to the centre of compartment n consists of the following components: a capacitive current, ion currents across the membrane and intracellular currents to neighbored compartments. Applying Kirchhoff's law for compartment n results in

$$\frac{d(V_{i,n} - V_{e,n})}{dt} \cdot C_n + I_{ion,n} + \frac{V_{i,n} - V_{i,n-1}}{R_n/2 + R_{n-1}/2} + \frac{V_{i,n} - V_{i,n+1}}{R_n/2 + R_{n+1}/2} = 0 \quad (1)$$

with intracellular potential V_i, axial resistance R and membrane capacity C. The following system of differential equations is deduced by introducing the transmembrane voltage $V = V_i - V_e$ to compute the time courses of V_n in every compartment (Rattay, 1999):

$$\frac{dV_n}{dt} = \left[-I_{ion,n} + \frac{V_{n-1} - V_n}{R_{n-1}/2 + R_n/2} + \frac{V_{n+1} - V_n}{R_{n+1}/2 + R_n/2} + \frac{V_{e,n-1} - V_{e,n}}{R_{n-1}/2 + R_n/2} + \frac{V_{e,n+1} - Ve,n}{R_{n+1}/2 + R_n/2} \right] \Big/ C_n. \quad (2)$$

The direct stimulating influence of the extracellular potential on compartment n is defined by the activating function (Rattay, 1999)

$$f_n = \left[\frac{V_{e,n-1} - V_{e,n}}{R_{n-1}/2 + R_n/2} + \frac{V_{e,n+1} - V_{e,n}}{R_{n+1}/2 + R_n/2} \right] \Big/ C_n. \quad (3)$$

For a fiber with constant diameter d, constant compartment length Δx, intracellular resistivity ρ_i and specific capacity c, (3) appears in a simpler form

$$f_n = \frac{d}{4c \cdot \rho_i} \cdot \frac{V_{e,n+1} - 2V_{e,n} + V_{e,n+1}}{\Delta x^2}. \quad (3a)$$

The value within the brackets of (3) corresponds to a virtual injected current applied to compartment n. In regions where this current is positive, the membrane depolarizes and where it is negative, it tends to hyperpolarize.

VOLTAGE SENSITIVE DYE IMAGING

Transverse hippocampal slices were obtained from P21 C57B6 mice as previously described (Leao et al., 2009) and according to the rules of Animal Experimentation of the Uppsala University. Slices were maintained in artificial ACSF (in mM: 124 NaCl, 3.5 KCl, 1.25 NaH_2PO_4, 1.5 $MgCl_2$, 1.5 $CaCl_2$, 30 $NaHCO_3$, 10 glucose), constantly bubbled with 95% O_2 and 5% CO_2. Recordings/imaging were obtained at 25 °C, in the presence of 10 μM CNQX, 30 μM dAP5 and 10 μM bicuculline methochloride to minimize the effect of synaptic currents (Leao et al., 2005). Voltage sensitive dye (VSD) loading (JPW3027 obtained from Prof Leslie Loew, University of Connecticut, USA) was performed exactly as described in Palmer and Stuart (2006). Images were acquired using a EM-CCD camera (Luca, Andor, Ireland). Excitation was produced by a 200W metal-halide lamp through a bypass filter centered at 535 nm (~510 to 560 nm pass) and emission was low-pass filtered at 590 nm. Image acquisition and extracellular stimulation were synchronized by a National Instruments digital device and to guarantee time precision, we recorded the stimulator and the camera 'fire' outputs (that flags image acquisition) using a National Instruments DAQ card. Current clamp recordings were also obtained from the imaged cell using winWCP (Dr John Dempster, Strathclyde University, UK). The stimulating electrode (tungsten, 10 μm tip) was placed 50 and 75 μm above axons. Pulses had 100 μs durations and extracellular current intensities were adjusted to 75% of the minimum threshold current. Images were taken 100 μs after the stimulus using 100 μs exposure. Pixel intensity was measured in 4 × 2 pixel region of interest and averaged from 10 images acquired with 1s delay between each other.

RESULTS

In the following several computer experiments are proposed to analyze step by step characteristics of strength–duration curves and related historical formulas.

Intracellular stimulation: space clamp versus cable model

In order to describe the neural excitation process independently from the intracellular current needed for spike conduction, Hodgkin et al. (1952) used the space clamp technique. They stimulated with a long inserted wire that clamped the squid axon uniformly along its entire length. An equivalent model situation is created by current injection into the soma of Neuron 1 by cutting all soma processes. Stimulation of the resting soma with a rather long weak pulse results in a transmembrane voltage curve $V(t)$ with an asymptotic exponential increase during the subthreshold response (Fig. 2A). The time constant for the exponential voltage of the passive membrane is the product of the ohmic resistance and the capacity of the cell membrane ($\tau = R \cdot C$). The time constant τ of such an exponential increase can be found graphically by linear extrapolation at stimulus onset as the intersection of the tangent in V at pulse onset with the steady state indicated by the horizontal dashed line in Fig. 2A. At the end of the 8 ms pulse, the subthreshold approach of V is very close to its stationary value.

The shape of the subthreshold membrane voltage $V(t)$ changes considerably when the stimulus current is allowed to flow not only across the membrane but also intracellularly from the stimulated soma into the dendrite and the axon. Finding τ by the graphical method of Fig. 2A becomes contradictory when applied in Fig. 2B and C as it results in shorter time values $t1$ while needing

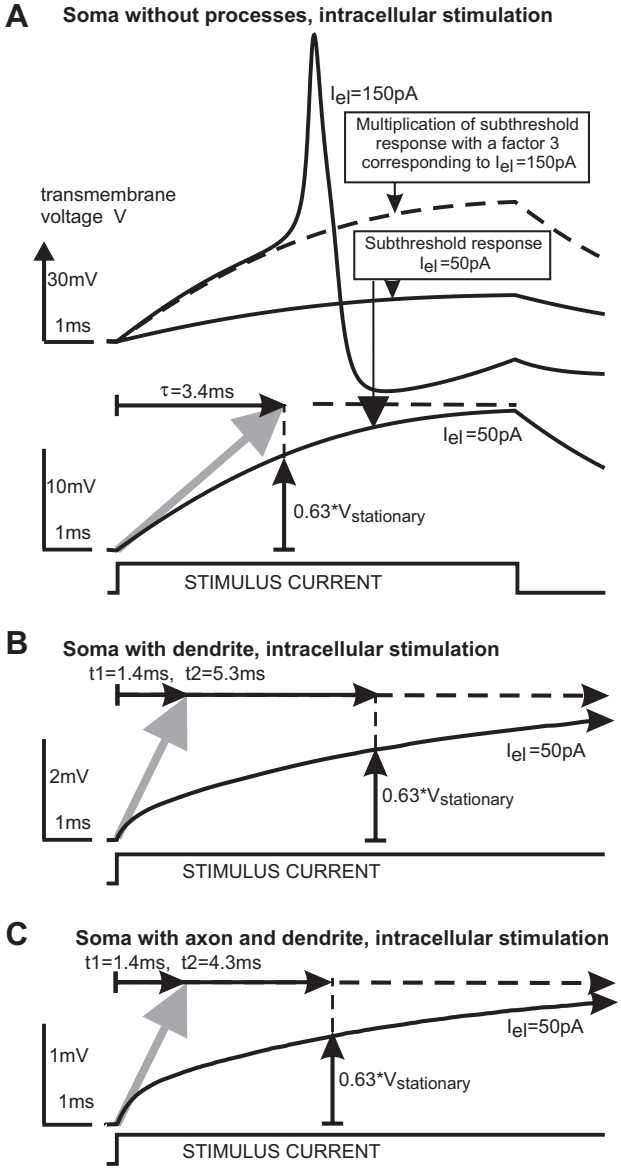

Fig. 2. Transmembrane voltage V of Neuron 1 for intracellular stimulation at the soma. (A) Space clamp condition with no axial current flow. The top graph demonstrates the coincidence of the passive and active membrane response in the subthreshold regime. Linear extrapolation of V at stimulus onset up to the steady state value of the single RC circuit (gray arrow) defines the time constant of the passive membrane response as $\tau = R \cdot C$ (lower graph of A). With the same electrode current I_{el} = 50 pA, the steady state value of V is reduced by a factor ~5 when axial current flows into the dendritic branch (B) and by a factor ~10 for conductance into dendrite and axon (C). In comparison with the space clamp condition, intracellular current flow into dendrite and axon results in shorter times $t1$ but longer times to reach the steady state of the subthreshold membrane.

longer times for reaching the steady state (pulse durations > 20 ms). Obviously, the fit by a single exponential function corresponding to a single RC element (as in case A, where 63% of $V_{stationary}$ is determined by τ) cannot describe the subthreshold response of the cable model in an acceptable way. We have to change the method and define the time constant as the time $t2$ when the cable model reaches 63% ($1 - 1/e$) of the stationary membrane voltage V (Fig. 2B and C). Note that the time constant of the cable model is not an average value of the time constants of the compartments. This is demonstrated by Fig. 2B where both the dendrite and the soma of Neuron1 have quite the same electric membrane properties. The main difference between τ and its replacing values $t1$ and $t2$ in Fig. 2A and B is a consequence of a distinctly reduced steady state membrane voltage when the greater part of the stimulus current flows into the dendrite. The different temporal excitation profiles shown in Fig. 2 have consequences on the corresponding strength–duration curves.

The middle solid line in Fig. 3 shows the strength–duration relation under the space clamp condition where chronaxie is independent from the soma area. Allowing part of the injected current to flow into dendrites and the axon demands for stronger threshold currents for all pulse durations (Fig. 3, upper solid line). The intracellular strength–duration curves for Neuron 1 and its space clamped version deviate in their shapes for long pulses. With the same electrical cell properties, the calculated intracellular chronaxie ratio 2.5/1.79 = 1.4 (Fig. 3) becomes smaller by enlargement of the soma surface or by reducing the number or diameters of processes. The variable chronaxie ratio decreases to 1 if the diameters of the soma processes converge to zero, which is the space clamp condition.

This dependence of chronaxie on diameter disproves the often applied rule mentioned in the introduction, namely chronaxie $\sim 0.7\tau$ with $\tau = R \cdot C$, where the product $R \cdot C$ is independent of membrane size. However, even more surprising is the huge deviation from this formula for extracellular stimulation. With the time constant of the soma membrane (Fig. 2A) we obtain chronaxie $\sim 0.7 \cdot 3.4$ ms = 2.38 ms instead of 0.38 ms for the case presented in Fig. 3.

In contrast to intracellular stimulation, in most applications extracellular stimulations are optimally achieved with cathodic currents (Ranck, 1975; Rattay, 1986, 1999). Hence, we compare anodic inside with cathodic outside stimulation in order to explain in the next subsections the large chronaxie differences between intra- and extracellular stimulation shown in Figs. 1B and 3.

Extracellularly activated region increases with electrode distance

A straight fiber with the properties of the naked axon of Neuron 1 is shown in Fig. 4A–C for external stimulation with a cathodic 100 μs pulse at threshold intensity. In contrast to intracellular stimulation, the externally positioned microelectrode causes in every compartment an injected virtual current. As second important effect, outside stimulation with a monophasic pulse produces virtual currents

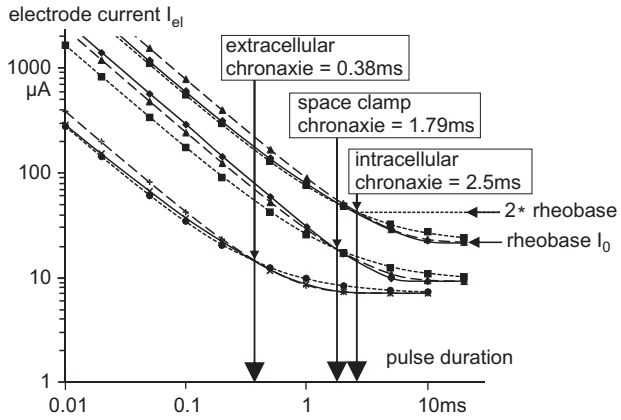

Fig. 3. Strength–duration curves of the somatic membrane of Neuron 1 for stimulation with square pulses. Chronaxie defined as the pulse duration needed for twice the rheobase I_0 (horizontal arrows) is different for the space clamp condition (central group of three curves) and the case of current flowing into dendrites and the axon (upper curves). Injected anodic current amplitudes (upper and central groups) are shown as current densities for 1 cm^2 membrane. Extracellular stimulation (lower curves) is with cathodic currents for a point source 50 μm above soma center. Approximation of the strength–duration curves according to the classical formulas of Lapicque (1907): $I_{el} = I_0/(1 - 2^{-k})$ (dashed lines) and Weiss (1901): $I_{el} = I_0(1 + 1/k)$ (dotted lines) where k is pulse duration/chronaxie.

of both polarities where the sum of all the virtual currents is zero.[1] The driving forces of excitation are the currents in the region with positive activating function values (red arrows in Fig. 4C).

The length of the region where a cathodic point source causes positive activating function is $\sqrt{2} * z_{el}$, where z_{el} is the electrode distance. This formula is correct for a straight nonmyelinated fiber with constant diameter in a homogeneous medium and the relation can be described by a 70-degree angle (Fig. 4A, $\tan(35°) = \sqrt{2}/2 * z_{el}/z_{el}$), (Rattay, 1986). According to the activating function concept, this angle is independent of fiber diameter and electrical membrane properties and can also be used as an approach for myelinated axons (Rattay, 1986). Large positive and negative isolated activating functions' values appear at locations with considerable diameter changes, in branching or in fiber endings. As axial intracellular currents level such local effects, the 70° rule is a rough approach even for these cases. A specific chronaxie value of a region can be expected as long as the zone defined by the 70° seen from the point source is concentrated in a cell region with common electrical properties.

The length of the activated portion flanked by the hyperpolarized regions increases with electrode–neuron distance, and consequently, the influence of the hyperpolarized region on the excitation process is gradually reduced when moving the current source away. This effect could be also demonstrated using VSD imaging.

[1] Eq. (1) is a current balance where the last two terms describe the intracellular current flow to the left and right neighboring compartments. Shifting to the next compartment ($n \rightarrow n + 1$) includes the 'old' right neighbor as new left neighbor, but the current flow has changed signs. Thus, the sum of these two currents is 0 and consequently the sum of all axial currents is 0. Applying this principle in Eq. (2) one find that the sum of all virtual stimulating currents is 0. For details see Rattay (1990).

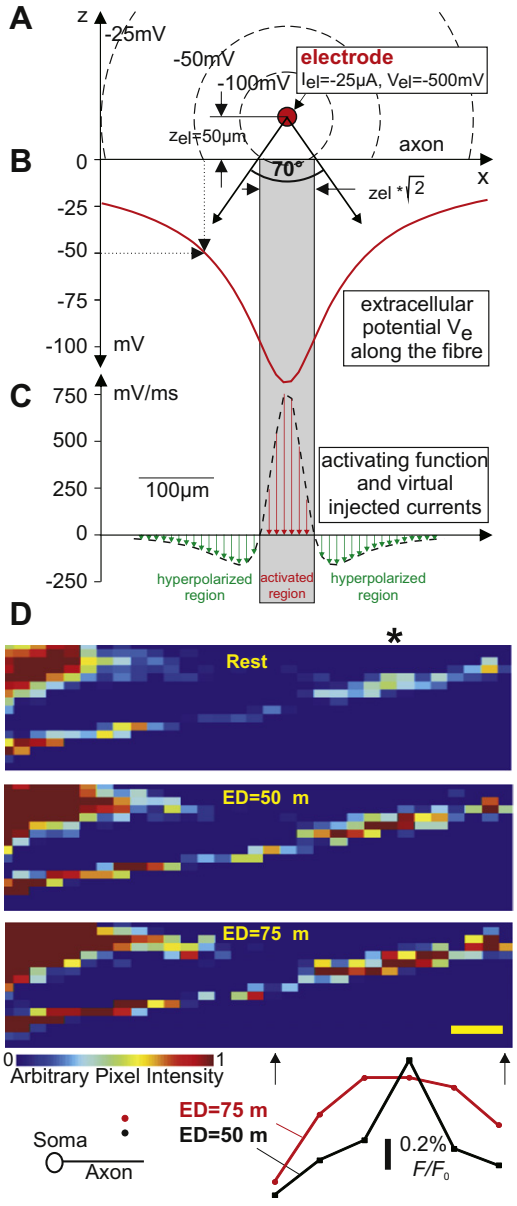

Fig. 4. Extracellular stimulation. (A) Geometry and isopotentials for a point source 50 µm above a fiber positioned at the *x*-axis. (B) Extracellular potential $V_e = \rho_e I_{el}/4\pi r$ with $r = \sqrt{(x - x_{el})^2 + z_{el}^2}$ is used to calculate the activating function. (C) A fiber with $d = 1$ µm and compartment length $\Delta x = 10$ µm results in a peak activating function value of 740 mV/ms. According to (2) this is the slope of the membrane voltage in the compartment below the electrode at the beginning of the −25 µA pulse. According to (3), the virtual currents are $f_n \cdot C_n$. With $C_n = d \cdot \pi \cdot \Delta x \cdot c = 3.14159 * 10^{-7}$ µF and specific membrane capacity c = 1 µF/cm^2, the maximum injected current is 232 pA at the center of the activated region. As the length of the activated region is defined by an angle of 70°, this region increases with electrode distance. (D) VSD imaging of a pyramidal cell axon at rest (upper photomicrograph), 100 µs after the stimulus for electrode distance $z_{el} = 50$ µm (middle photomicrograph) and $z_{el} = 75$µm (lower photomicrograph) (scale bar = 10 µm; * electrode position in the horizontal axis). Fluorescent traces for $z_{el} = 50$ and 75 µm versus axon position is shown below the photomicrographs and are aligned to the region in the axon activated by the extracellular stimulus. Each point in the traces represents average fluorescence of an axon region of approx. 10 µm length in five images.

The length of the depolarization detected by the intracellular VSD increases with electrode distance (Fig. 4D). The area under the curve in fluorescence (normalized by the maximum) versus length graph was used as a measurement of depolarization 'spread' caused by the extracellular stimulus. When the stimulating electrode was placed 50 µm ($z_{el} = 50$ µm) above the axon, the fluorescence ($\Delta F/F_0$, normalized) versus length integral was equal to 0.038 ± 0.002 µm^{-1} and 0.058 ± 0.004 µm^{-1} for $z_{el} = 75$ µm ($n = 5$ cells, $p = 0.008$, paired *t* test).

Intracellular versus extracellular stimulation

The spatio-temporal evolution of transmembrane voltage profiles is significantly different for a microelectrode positioned either above or in the soma (Fig. 5A–D). In Fig. 5A and B, pulse duration is 100 µs and membrane voltages along the neural axis are compared for threshold intensity. At the end of the pulse, extracellular stimulation shows a larger voltage maximum, but a shorter depolarized region. For 1 ms threshold pulses the same voltage profiles appear again with smaller amplitudes (due to lower stimulation currents) as the firsts of ten advancing 100 µs time steps (thick lines in Fig. 5C and D). The rather constant increase of the maximum and spatial extension of the voltage profile for the case of intracellular stimulation in the advancing 100 µs time steps demonstrate that intracellular stimulation is more effective as the injected current is available to load the membrane capacity in the vicinity of the electrode (Fig. 5D). Virtual negative injected currents during pulse application (Eq. (3)) cause strong hyperpolarization (Fig. 5A and C). An essential part of the virtual positive current, the driving force for excitation, is lost as a result of the counterbalancing axial current flow between the depolarized and the two hyperpolarized regions. Note that half of the positive voltage profile (its extension and maximum value) is already reached at approx. 10% of the 1 ms stimulation pulse (thick line in Fig. 5C). This is contrary to the gradual increase of the voltage profile seen in Fig. 5D.

A second important effect is demonstrated in the 10 ms pulse example (Fig. 6). The subthreshold response for extracellular stimulation has a maximum at half of the stimulus pulse time with a decay related to the inactivation gating variable *h* (Mainen et al., 1995) that act as a factor for the sodium current[2] (Fig. 6A). The quicker extracellularly elicited voltage increase affects the lower *h* values. The maximum appears earlier for extracellular electrode positions above AIS and node of Ranvier (Fig. 6C). In contrast, Fig. 6B and D shows a rather constant increase in membrane voltages indicating that stimulation is still possible with longer and weaker pulses.

Chronaxie increases with electrode distance

In the previous section and with Fig. 3, it was demonstrated that axial current flow from the activated area into

[2] Sodium current, the driving component in excitation, is modeled as $g_{Na} m^3 h (V - E_{Na})$, with maximum conductance g_{Na}, gating variables *m* and *h*, membrane voltage *V* and Nernst potential E_{Na}. In the resting state *m* has a quite small value in contrast to the inactivation variable *h* which starts with a high value that decreases (with some delay) when *V* increases.

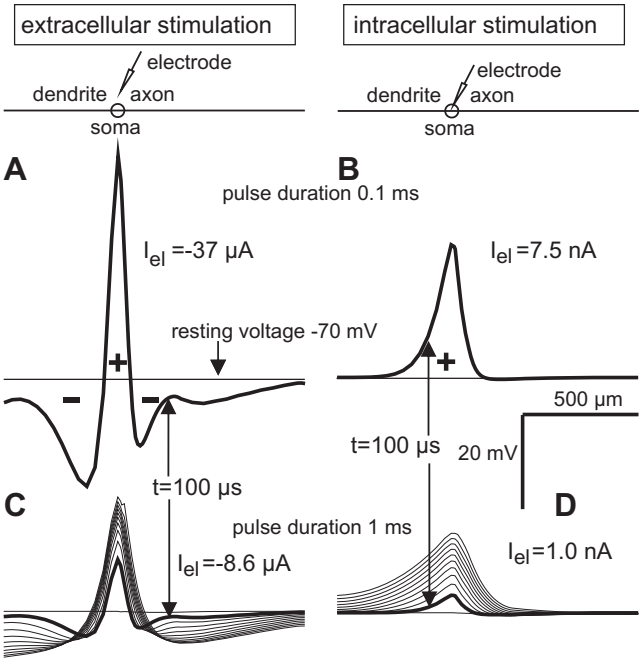

Fig. 5. Spatial transmembrane voltage profiles for extra- and intracellular stimulation computed for Neuron 1. Extracellular stimulation 50 µm above the soma (A, C) with cathodic threshold currents. Corresponding intracellular anodic threshold current cases at the right side (B, D). Voltage along the neural axis at the end of a 100 µs stimulation pulse (A, B) and in ten advancing 100 µs time steps for a 1 ms stimulation pulse (C, D).

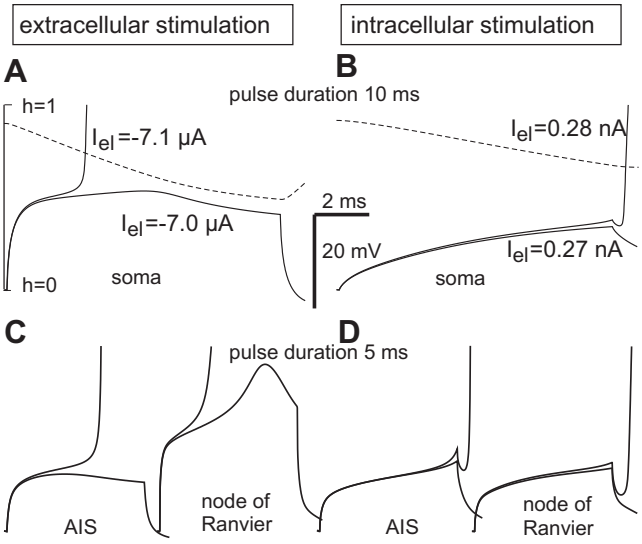

Fig. 6. Comparison of threshold and subthreshold membrane voltages as functions of time of the compartments closest to the electrode, computed for Neuron 1. Extracellular cathodic stimulation 50 µm above soma (A), AIS and node of Ranvier (C). Corresponding intracellular anodic stimulation at the right side. The dashed lines in A and B show the inactivation gating variable *h* for subthreshold cases; note its quicker decay and the lower minimum for extracellular stimulation. During pulse application there is a monotonous voltage increase in all intracellularly stimulated cases, whereas extracellular stimulation causes a maximum in every of the subthreshold voltage curves, most pronounced in the node of Ranvier example. As shown in A, the maximum is a consequence of the decreasing inactivation variable *h*. Pulses loose their stimulating properties as soon as the maximum is reached. Same scaling in all graphs.

the hyperpolarized regions causes shorter chronaxies for cathodic extracellular than for intracellular stimulation. It was also shown that the activated length is related to an angle of 70° at the electrode and this activated length increases with microelectrode distance (Fig. 4). Consequently, stimulating current loss along the neural axis into the side lobes as defined by the activating function shows a reduction when intracellular resistance between depolarized and hyperpolarized regions increases by increasing electrode distance. Comparison of excitation profiles for electrodes at 50 and 200 µm above the soma (Fig. 7) emphasizes the trend to longer chronaxies for larger electrode distances. As seen in the case at 200 µm above the soma, the larger distance between the primarily

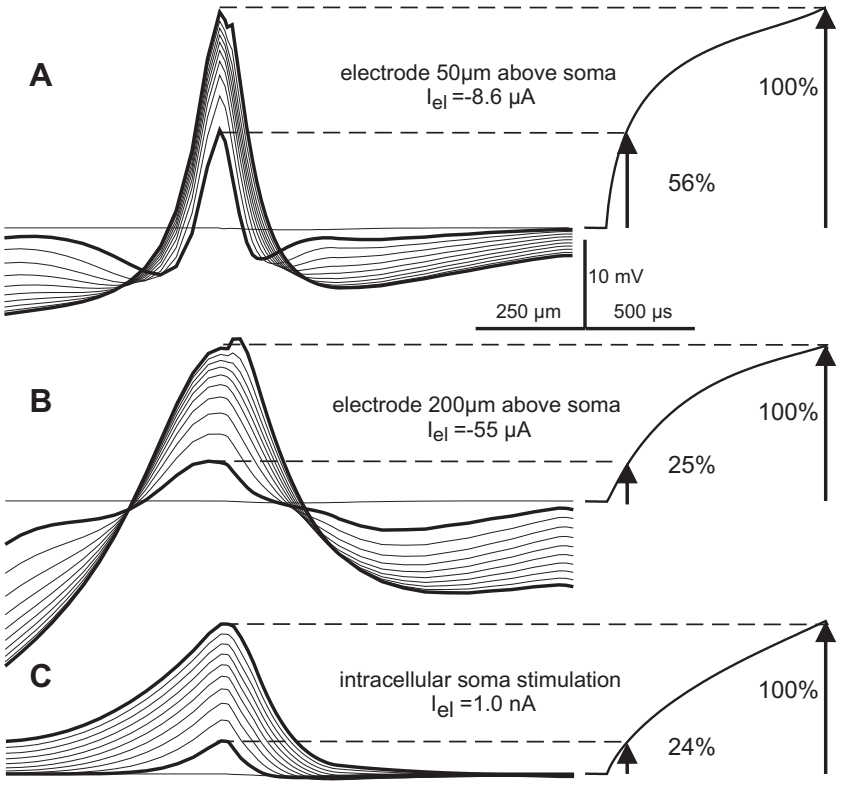

Fig. 7. Temporal evolution of transmembrane voltage profiles in 100 µs time steps during a 1 ms pulse at threshold stimulation above the soma (left) and soma membrane voltage as a function of pulse time (right). In case A, 56% of the transmembrane voltage is already reached after the first 100 µs. Increasing the electrode distance from z_{el} = 50 µm (A) to z_{el} = 200 µm (B) causes a similar and consistent voltage increase as for intracellular stimulation. For both cases approx. 25% of the transmembrane voltages are reached after the first 100 µs (C) Left figures A and C are replications of Fig. 5C and D.

depolarized and hyperpolarized regions results in a more constant increase of the voltage profile which becomes comparable to that of the intracellular case.

Strength–duration curves for electrode positions above the soma and a node of Ranvier underline the association of increasing chronaxies with increasing electrode distance (Fig. 8). Chronaxie was determined by the intersection of strength–duration curves with the horizontal line 2^* rheobase, with electrode currents normalized to rheobase (Fig. 8). The lower part of the figure uses the chronaxie values of the shown strength–duration curves for electrode distances of 50, 100, 200 and 300 µm to quantitatively describe chronaxie versus distance relationships for electrodes above the third node of Ranvier and the soma. For the extracellular stimulation cases, when increasing electrode distance, different functional neural parts become excited. For this reason, and more remarkably for the soma case, the curves containing the circles deviate from the direction pointed by the arrows (Fig. 8, bottom). Note the quite large difference between intra- and extracellular chronaxies.

A shift of the spike initiation zone by electrode distance increase is analyzed in the next example with two electrode positions at z_{el} = 50 µm and z_{el} = 200 µm above the center of the naked axon of Neuron 1 (Fig. 9). In contrast to the 50 µm case (A) the depolarized region predicted by the activating function with the 70-degree angle (Fig. 4) exceeds the 200 µm long naked axon for z_{el} = 200 µm. There is a change in the sign of the slopes at the onset of the 200 µs stimulus within the naked axon region in (A), whereas for z_{el} = 200 µm the slopes are always positive in the larger region marked by the gray rectangle indicating the activated region (Fig. 9B). In case B, the activating function values at the border between AIS and the naked axon are essentially smaller than below the electrode. However, the high sodium channel density of AIS supports spike initiation at the naked axon, acting as a favorable neighboring compartment. The activating function values for the AIS are very similar to those values for the naked axon close to it, but its position next to the soma results unfavorable. The convenient neighboring compartments together with axial current flow are crucial components for excitation during intra- and extracellular stimulation.

In the next section we show that in some cases axial current flow initiates spikes rather far away from the stimulating electrode when long pulses are applied whereas for short pulses spike initiation is close to the electrode. By systematic evaluation and analysis of computer simulations we discovered this phenomenon with remarkable consequences for strength–duration curves.

Deviations from classical strength–duration curves

In order to smoothen recording errors, strength–duration curves are usually fitted by one of the classical

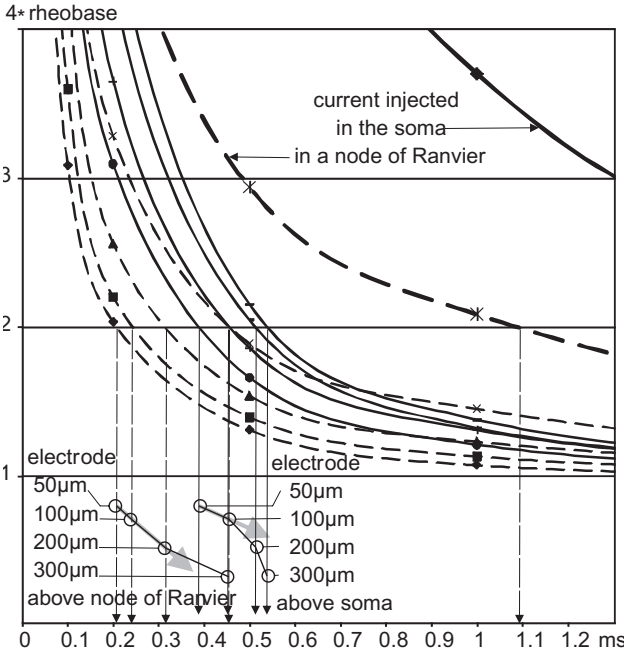

Fig. 8. Strength–duration curves for Neuron 1 normalized to rheobase for electrodes above the soma (solid lines) and the third node of Ranvier (broken lines). Chronaxies marked by vertical arrows increase with electrode–cell axis distance toward the value for inside stimulation (marked by thick lines) which is 1.1 ms for the third node of Ranvier (comp. Fig. 1B) and 2.6 ms for the soma. The circles in the lower part of the figure help to identify the strength–duration curves. The curves containing the circles show a trend toward larger chronaxies with increasing electrode distances.

approaches, the formulas of Weiss and Lapicque (Fig. 3). However, for a constant electrode position our computer simulations demonstrate that deviations from these curves have to be expected when spikes are initiated at different functional parts for short and long pulses. Intracellular stimulation of the main dendrite of Neuron 2 results in a composite strength–duration curve. This curve consists of two segments of 'classical curves' that are connected with a transition part (thick red curve marked as DEND in the lower part of Fig. 1B, the case of intracellular stimulation).

The occurring phenomena for this main dendrite and other neural structures are explained extensively in Fig. 10. For short pulses, spikes are generated within the dendrite at the site of current injection (green curve in Fig. 10A). As expected, but not shown, the spike bifurcates there with one part conducted toward the axon and the other toward peripheral dendritic regions. For a longer stimulation pulse of 5 ms, during the first part of stimulation spatial transmembrane voltage distributions similar to the green curve are produced at subthreshold intensity, but with smaller amplitudes (e.g., the two thick blue lines in Fig. 10A). During a 5 ms pulse just above threshold intensity, the peak value at this electrode position is not strong enough to produce a dendritic spike, but axial current flow into the axon causes enough sodium current via the low threshold sodium channels Nav1.6 in AIS. As a result a spike initiates at the beginning of the thin part of the axon (t = 5.7 ms, lower thin blue line in Fig. 10A).

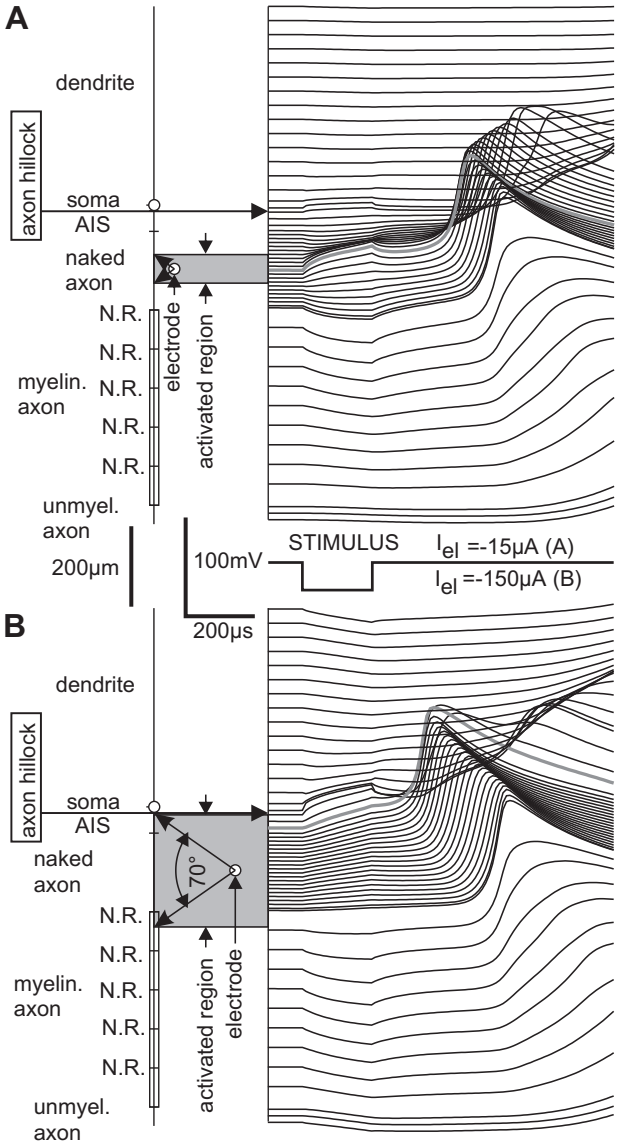

Fig. 9. Stimulation of Neuron 1 by a microelectrode 50 µm (A) and 200 µm (B) above the center of the naked axon. Every line on the right side shows the membrane voltage of one compartment in accordance with the cell geometry (left). Short compartment lengths in the unmyelinated axon are because of numerical reasons. Thick gray lines represent the membrane voltage where spikes are initiated which is at the center of the naked axon corresponding to the electrode position in A but is shifted into AIS in B.

Thereafter, this spike bifurcates in an asymmetric way because of asymmetric cell properties.

In the presented examples of extracellular stimulation, the effect of combined strength–duration curves is difficult to observe for cathodic currents, although the phenomenon is present in a weak form for the cases SOMA and DEND (upper part of Fig. 1B). In contrast, combined strength–duration curves occurs clearly for anodic pulses (Fig. 10B), especially for an electrode above the soma or a node of Ranvier. In contrast to cathodic stimulation, anodic stimulation generates a center of hyperpolarization at a region of the neuron closest to the electrode, and the side lobes of the activating function (marked in Fig. 4 by green arrows) became the driving forces for excitation.

Therefore, the first reaction describing the membrane voltage after 10 µs of anodic stimulation for an electrode at 50 µm above the soma has two positive peaks (Fig. 10C, black line). Short pulses cause spike initiation at the distal end of the AIS (Fig. 10C, green curves), whereas spikes arise at the centre of the thin axonal segment for long pulses (Fig. 10C, blue curves). A similar shift phenomenon occurs when the electrode is above the third node of Ranvier (Fig. 10D): spikes are initiated at the distal end of the thin segment and at a position closer to its center by short and long pulses, respectively.

DISCUSSION

The time constant of a patch of cell membrane is defined as $\tau = R \cdot C$, with capacity C and resistance R. Chronaxie

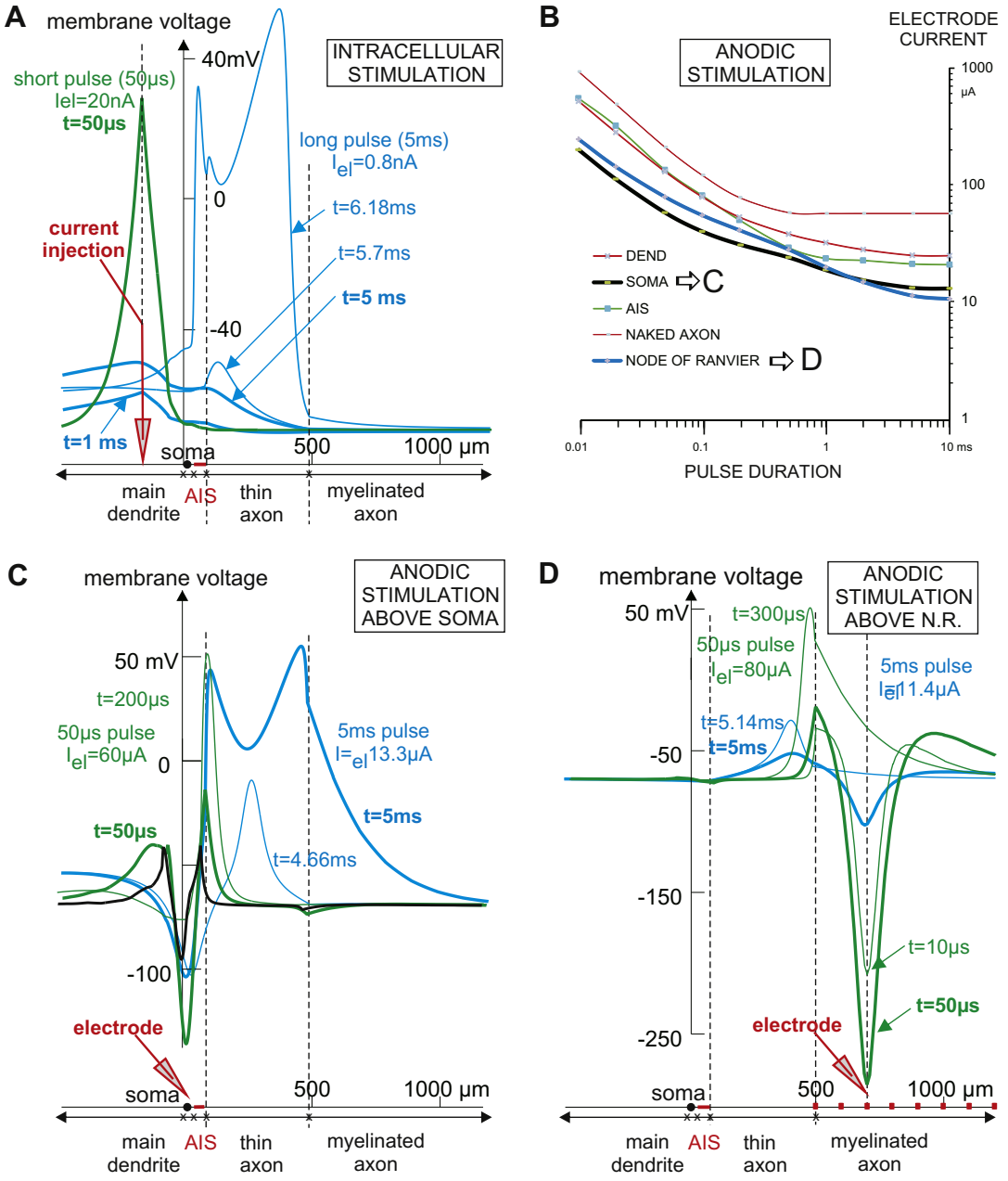

Fig. 10. Spike initiation sites change for short and long current pulses. Dashed vertical lines indicate electrode position, end of AIS and the beginning of myelination. Membrane voltages profiles are shown for 50 µs (green) and 5 ms (blue) pulse stimulation at selected times. (A) Intracellular stimulation of Neuron 2 at the main dendrite. At the end of a 50 µs pulse with threshold intensity (20 nA) a dendritic spike (green curve) is generated. Although during a 5 ms pulse just above the 0.79 nA threshold the maximum membrane potential occurs close to the electrode position (thick blue curves), the spike arises at a quite distant position (~300 µm) at the thin segment of the axon. (B–D) Extracellular anodic stimulation of Neuron 2 for electrode positions as defined in Fig. 1A. (B) Electrode positions above the soma (black line) and the third node of Ranvier (blue line) cause combined strength–duration curves as spike initiation site depends on pulse duration in these cases. (C) Stimulus electrode above soma. Thick lines show the situation at the end of the pulses. For better recognition the 10 µs response of the short pulse stimulation is shown in black. (D) Stimulus electrode above node of Ranvier.

is about 0.7τ for such a patch (Ranck, 1975; Reilly, 1992) which is independent of cell geometry as long as intracellular axial current flow is negligible. The large variety in membrane resistance is the main reason for specific chronaxie values for different functional unmyelinated cell regions. In contrast to the variance found in membrane resistance, membrane capacity is rather uniform with a value close to 1 $\mu F/cm^2$ (Cole, 1968). However, myelinated regions have considerably smaller chronaxies as the total membrane capacity is inversely proportional to the number of myelin sheets.

Strength–duration characteristics for external stimulation of myelinated peripheral axons can be derived with linear methods from the intracellular relationship (Warman et al., 1992). In contrast to peripheral nerve applications, microelectrodes for central nervous system stimulation operate often in or in the vicinity of the soma, where additional effects appear as consequences of the variation of the electrical and geometrical parameters along the neural axis.

Here, we have demonstrated a radical switch to short chronaxies when the stimulating electrode position changes from inside to outside the cell. The inside/outside chronaxie ratio with a value close to 6.5 was the largest for the smallest investigated cell–electrode distance of 50 μm (Fig. 8). This ratio depends essentially on the length of the excited zone positioned between hyperpolarized regions for the cathodic case. These hyperpolarizing lobes hinder the continuous excitation process seen by intracellular stimulation. Consequently, the inside/outside chronaxie ratio becomes smaller for larger electrode–cell distances. Increasing electrode distance usually will cause the excitation of other functional cell regions with other chronaxic properties. This phenomenon is especially obvious for the electrode position above a soma with highly excitable neighbored axonal regions showing shorter chronaxies (upper part of Fig. 1B), and therefore, the measured chronaxie cannot just reflect the somatic value, but a value influenced by the excited axonal region. This chronaxie mix disturbs the original trend toward chronaxie values for intracellular stimulation as marked by gray arrows in the lower part of Fig. 8.

The presented theory predicts the experimentally observed trend to larger chronaxies for increased distances (West and Wolstencroft, 1983). An analytical approach is available for non-myelinated nerve and muscle fibers that predicts different chronaxies for intra- and extracellular stimulation and the increase of chronaxie with electrode–fiber distance (Suarez-Antola, 2005).

Examples of combined strength–duration curves have been presented where short and long pulses cause spike initiation in different cell regions. Thus, fitting strength–duration data with a single curve according to the classical approaches of Weiss or Lapique may be equivocal. Some combined strength–duration curves resulting from retinal ganglion cell recordings can be found in Fig. 9 of Gerhardt et al. (2011).

Our results help explain trends of strength–duration characteristics. For example, Neuron 1 and Neuron 2 have comparable strength–duration curves with similar excitability sequences (node-ais-soma-dend) both for intra- and extracellular stimulation (Fig. 1B). However, unexpected differences between both neurons occur, e.g., only Neuron 2 shows a bimodal intracellular strength–duration curve (red thick curve in the lower part of Fig. 1B).

It is important to notice that many variables like synaptic activity (Spruston, 2008; Sjöström et al., 2008), refractory behavior (Miocinovic and Grill, 2004), inhomogeneity in ion channel density (Migliore and Shepherd, 2002; Keren et al., 2009), branching (Manita and Ross, 2009), curvature of axons (Rattay et al., 2000; Iles, 2005), pulse shape (Wongsarnpigoon et al., 2010), electrode configurations (Smith and Finley, 1997), the inhomogeneity and anisotropy in the tissue (Roth, 1995), pulse trains and neuromodulation (De Vries et al., 2007; Minassian et al., 2007) can influence recruitment and strength–duration relationships. Nevertheless, by applying careful analysis, the large variance in chronaxie, even within one cell should be helpful for selective stimulation, especially when microelectrodes are used to activate a specific region like the AIS, a part of the dendritic tree or the myelinated axon. As an example, short pulse widths selectively activate cells with their somas close to the electrode in epiretinal stimulation (Behrend et al., 2011).

One should be aware that chronaxie is also the time where stimulus pulse duration needs a minimum of energy (Geddes, 2004), an important fact for neural prostheses. Moreover, charge injection (electrode current times pulse duration) from electrode surface limits neural prosthetic applications. The left (quite) linear part of double logarithmic strength–duration curves, e.g. in Fig. 1B, predicts (nearly) constant charges when thresholds of very short pulses are compared (half pulse duration needs double threshold current). Minimum charge occurs with infinitely short pulse duration. With the approach of Weiss (Fig. 3) the factor for the additional charge costs are pulse duration divided by chronaxie.

CONCLUSIONS

A recent review and several often cited articles sustain the wrong dogma that chronaxie is the same for intra- and extracelluar stimulation (Borchers et al., 2012; Nowak and Bullier, 1998; Geddes, 2004). On the contrary, evaluations of our compartment model of a cortical pyramidal cell demonstrate up to 20 times longer chronaxies for intracellular stimulation than for extracellular stimulation (Fig. 1B). This fact as well as the occurrence of combined strength–duration curves are supported by theoretical investigations.

Acknowledgments—We thank Dr. Katarina Leao for meaningful comments in earlier versions of this manuscript. This work was supported by the Austrian Science Fund, Grant No. 21848-N13. R.N.L. is supported by a Kjell and Märta Beijers Foundation Grant.

REFERENCES

Behrend MR, Ahuja AK, Humayun MS, Chow RH, Weiland JD (2011) Resolution of the epiretinal prosthesis is not limited by electrode size. IEEE Trans Neural Syst Rehabil Eng 19:436–442.

Blair HA (1932) On the measure of excitability. J Gen Physiol 16:165–175.

Boinagrov D, Loudin J, Palanker D (2010) Strength–duration relationship for extracellular neural stimulation: numerical and analytical models. J Neurophysiol 104:2236–2248.
Borchers S, Himmelbach M, Logothetis N, Karnath H (2012) Direct electrical stimulation of human cortex – the gold standard for mapping brain functions? Nature Rev Neurosci 13:63–70.
Brindley GS (1955) The site of electrical excitation of the human eye. J Physiol 127:189–200.
Carnevale NT, Hines ML (2006) The NEURON book. Cambridge, UK: Cambridge University Press.
Cohen ED (2007) Prosthetic interfaces with the visual system: biological issues. J Neural Eng 4:R14–R31.
Cole KS (1968) Membranes, ions and impulses. Berkley: University of California Press.
De Vries J, De Jongste MJ, Spincemaille G, Staal MJ (2007) Spinal cord stimulation for ischemic heart disease and peripheral vascular disease. Adv Tech Stand Neurosurg 32:63–89.
Dowling J (2005) Artificial human vision. Expert Rev Med Devices 2:73–85.
Fernández E, Pelayo F, Romero S, Bongard M, Marin C, Alfaro A, Merabet L (2005) Development of a cortical visual neuroprosthesis for the blind: the relevance of neuroplasticity. J Neural Eng 2:R1–R12.
Fried SI, Hsueh HA, Werblin FS (2006) A method for generating precise temporal patterns of retinal spiking using prosthetic stimulation. J Neurophysiol 95:970–978.
Fried SI, Lasker AC, Desai NJ, Eddington DK, Rizzo 3rd JF (2009) Axonal sodium-channel bands shape the response to electric stimulation in retinal ganglion cells. J Neurophysiol 101: 1972–1987.
Geddes LA (2004) Accuracy limitations of chronaxie values. IEEE Trans Biomed Eng 51:176–181.
Gerhardt M, Groeger G, MacCarthy N (2011) Monopolar vs. bipolar subretinal stimulation – an in vitro study. J Neurosci Methods 199:26–34.
Greenberg RJ, Velte TJ, Humayun MS, Scarlatis GN, Juan E (1999) A computational model of electrical stimulation of the retinal ganglion cell. IEEE Trans Biomed Eng 46:505–514.
Hines ML, Morse T, Migliore M, Carnevale NT, Shepherd GM (2004) ModelDB: a database to support computational neuroscience. J Comput Neurosci 17(1):7–11.
Hodgkin AL, Huxley AF, Katz B (1952) Measurement of current–voltage relations in the membrane of the giant axon of Loligo. J Physiol 115:424–448.
Holsheimer J, Buitenweg JR, Das J, de Sutter P, Manola L, Nuttin B (2011) The effect of pulse width and contact configuration on paresthesia coverage in spinal cord stimulation. Neurosurgery 68:1452–1461.
Horsager A, Greenwald SH, Weiland JD, Humayun MS, Greenberg RJ, McMahon MJ, Boynton GM, Fine I (2009) Predicting visual sensitivity in retinal prosthesis patients. Invest Ophthalmol Vis Sci 50:1483–1491.
Hu W, Tian C, Li T, Yang M, Hou H, Shu Y (2009) Distinct contributions of Nav1.6 and Nav1.2 in action potential initiation and backpropagation. Nat Neurosci 12:996–1002.
Iles JF (2005) Simple models of stimulation of neurones in the brain by electric fields. Prog Biophys Mol Biol 87:17–31.
Jensen RJ, Ziv OR, Rizzo 3rd JF (2005) Thresholds for activation of rabbit retinal ganglion cells with relatively large, extracellular microelectrodes. Invest Ophthalmol Vis Sci 46:1486–1496.
Keren N, Bar-Yehuda D, Korngreen A (2009) Experimentally guided modelling of dendritic excitability in rat neocortical pyramidal neurones. J Physiol 587:1413–1437.
Lapicque L (1907) Recherches quantitatives sur l'excitation électrique des nerfs traitée comme une polarisation. J Physiol Pathol Gen 49:620–635.
Lapicque L (1929) The chronaxic switching in the nervous system. Science 70:151–154.
Leao RN, Leao FN, Walmsley B (2005) Non-random nature of spontaneous mIPSCs in mouse auditory brainstem neurons revealed by recurrence quantification analysis. Proc Biol Sci 272:2551–2559.
Leao RN, Tan HM, Fisahn A (2009) Kv7/KCNQ channels control action potential phasing of pyramidal neurons during hippocampal gamma oscillations in vitro. J Neurosci 29:13353–13364.
Mainen ZF, Joerges J, Hugenard JR, Sejnowski TJ (1995) A model of spike initiation in neocortical pyramidal neurons. Neuron 15:1427–1439.
Manita S, Ross WN (2009) Synaptic activation and membrane potential changes modulate the frequency of spontaneous elementary Ca^{2+} release events in the dendrites of pyramidal neurons. J Neurosci 29:7833–7845.
Migliore M, Shepherd GM (2002) Emerging rules for the distributions of active dendritic conductances. Nat Rev Neurosci 3:362–370.
Minassian K, Persy I, Rattay F, Pinter MM, Kern H, Dimitrijevic MR (2007) Human lumbar cord circuitries can be activated by extrinsic tonic input to generate locomotor-like activity. Hum Mov Sci 26:275–295.
Miocinovic S, Grill WM (2004) Sensitivity of temporal excitation properties to the neuronal element activated by extracellular stimulation. J Neurosci Methods 132:91–99.
Nowak LG, Bullier J (1998) Axons, but not cell bodies, are activated by electrical stimulation in cortical gray matter. I: Evidence from chronaxie measurements. Exp Brain Res 118:477–488.
Palmer LM, Stuart GJ (2006) Site of action potential initiation in layer 5 pyramidal neurons. J Neurosci 26:1854–1863.
Pezaris JS, Reid RC (2009) Simulations of electrode placement for a thalamic visual prosthesis. IEEE Trans Biomed Eng 56:172–178.
Ranck JB (1975) Which elements are excited in electrical stimulation of mammalian central nervous system: a review. Brain Res 98:417–440.
Rattay F (1986) Analysis of models for external stimulation of axons. IEEE Trans Biomed Eng 33:974–977.
Rattay F (1987) Ways to approximate current–distance relations for electrically stimulated fibers. J Theor Biol 125:339–349.
Rattay F (1990) Electrical nerve stimulation: theory, experiments and applications. Vienna: Springer.
Rattay F (1999) The basic mechanism for the electrical stimulation of the nervous system. Neuroscience 89:335–346.
Rattay F, Minassian K, Dimitrijevic MR (2000) Epidural electrical stimulation of posterior structures of the human lumbosacral cord. 2: Quantitative analysis by computer modeling. Spinal Cord 38:473–489.
Rattay F, Resatz S (2004) Effective electrode configuration for selective stimulation with inner eye prostheses. IEEE Trans Biomed Eng 51:1659–1664.
Rattay F, Wenger C (2010) Which elements of the mammalian central nervous system are excited by low current stimulation with microelectrodes? Neuroscience 170:399–407.
Reilly JP (1992) Electrical stimulation and electropathology. Cambridge, USA: Cambridge University Press.
Roth BJ (1995) A mathematical model of make and break electrical stimulation of cardiac tissue by a unipolar anode or cathode. IEEE Trans Biomed Eng 42:1174–1184.
Rushton WAH (1927) The effect upon the threshold for nervous excitation of the length of nerve exposed, and the angle between current and nerve. J Physiol 63:357–377.
Sekirnjak C, Hottowy P, Sher A, Dabrowski W, Litke AM, Chichilnisky EJ (2008) High-resolution electrical stimulation of primate retina for epiretinal implant design. J Neurosci 28:4446–4456.
Shepherd RK, Hardie NA, Baxi JH (2001) Electrical stimulation of the auditory nerve: single neuron strength–duration functions in deafened animals. Ann Biomed Eng 29:195–201.
Sjöström PJ, Rancz EA, Roth A, Häusser M (2008) Dendritic excitability and synaptic plasticity. Physiol Rev 88:769–840.
Smith DW, Finley CC (1997) Effects of electrode configuration on psychophysical strength–duration functions for single biphasic electrical stimuli in cats. J Acoust Soc Am 102:2228–2237.
Spruston N (2008) Pyramidal neurons: dendritic structure and synaptic integration. Nat Rev Neurosci 9:206–221.

Stuart G, Spruston N, Sakmann B, Häusser M (1997) Action potential initiation and backpropagation in neurons of the mammalian CNS. Trends Neurosci 20:125–131.

Suarez-Antola RE (2005) The time constants for the electric stimulation of nerve and muscle fibers by point electrodes. In: Proceeding of the 2nd IEEE EMBS conference on neural engineering. Arlington, Virginia, pp. 652–655.

Tehovnik EJ, Slocum WM, Smirnakis SM, Tolias AS (2009) Microstimulation of visual cortex to restore vision. Prog Brain Res 175:347–375.

Voorhees CR, Voorhees 3rd WD, Geddes LA, Bourland JD, Hinds M (1992) The chronaxie for myocardium and motor nerve in the dog with chest-surface electrodes. IEEE Trans Biomed Eng 39:624–628.

Warman EN, Grill WM, Durand D (1992) Modeling the effects of electric fields on nerve fibers: determination of excitation thresholds. IEEE Trans Biomed Eng 39:1244–1254.

Weiss G (1901) Sur la possibilité de rendre comparables entre eux les appareils servant a l'excitation électrique. Arch Ital Biol 35:413–446.

West DC, Wolstencroft JH (1983) Strength–duration characteristics of myelinated and non-myelinated bulbospinal axons in the cat spinal cord. J Physiol 337:37–50.

Wongsarnpigoon A, Woock JP, Grill WM (2010) Efficiency analysis of waveform shape for electrical excitation of nerve fibers. IEEE Trans Neural Syst Rehabil Eng 18:319–328.

Yu Y, Shu Y, McCormick DA (2008) Cortical action potential backpropagation explains spike threshold variability and rapid-onset kinetics. J Neurosci 28:7260–7272.

Zrenner E (2002) Will retinal implants restore vision? Science 295:1022–1025.

(Accepted 5 April 2012)
(Available online 16 April 2012)